Comprehensive Analysis of Graphene Geometric Diodes: Role of Geometrical Asymmetry and Electrostatic Effects

D. Truccolo, P. Palestri, *Senior Member, IEEE*, D. Esseni, *Fellow, IEEE*, S. Boscolo, and M. Midrio

***Abstract*— A self-consistent Monte Carlo/3-D Poisson simulator has been developed to analyze the current asymmetry in graphene geometric diodes. The model couples ballistic transport in the graphene layer with 3-D electrostatics in the graphene and oxide substrate. Results are given in terms of transmission coefficients and currents at the two terminals of the diode. We prove that while the current asymmetry is mainly induced by ballistic transport in the asymmetric structure, the electrostatics plays a relevant role that tends to substantially counterbalance the geometrical effect.**

***Index Terms*— Ballistic transport, graphene, Monte Carlo.**

I. Introduction

GEOMETRIC diodes in graphene are attracting increasing interest from the scientific community due to their potential for novel applications in electronics and photonics [1]. Geometric diodes operate based on a pure ratchet effect [3]. They lack built-in potentials and space charge regions, resulting in extremely low capacitance, even down to attofarads [2]. These diodes can achieve frequency response in the THz range [4]. Hence, geometric diodes have a significant technological potential, especially in emerging THz technologies crucial for various applications across fields [5]. These applications include security screening [6], medical imaging [7], material analysis [8], and wireless communications [9].

Manuscript received 8 December 2023; revised 16 December 2023; accepted 19 December 2023. Date of publication 8 January 2024; date of current version 24 January 2024. This project has received funding from the European Union's Horizon 2020 research and innovation programme under grant agreement No 101006963 (GreEnergy). The review of this article was arranged by Editor K. Alam. *(Corresponding author: M. Midrio.)*

D. Truccolo, D. Esseni, and S. Boscolo are with the Dipartimento Politecnico di Ingegneria e Architettura (DPIA), University of Udine, 33100 Udine, Italy.

P. Palestri was with the Dipartimento Politecnico di Ingegneria e Architettura (DPIA), University of Udine, 33100 Udine, Italy. He is now with the Dipartimento di Ingegneria Enzo Ferrari, University of Modena and Reggio Emilia, 41125 Modena, Italy.

M. Midrio is with the Dipartimento Politecnico di Ingegneria e Architettura (DPIA), University of Udine, 33100 Udine, Italy, and also with CNIT, Consorzio Nazionale Italiano Telecomunicazioni, Udine, Italy (e-mail: midrio@uniud.it).

Color versions of one or more figures in this article are available at https://doi.org/10.1109/TED.2023.3347209.

Digital Object Identifier 10.1109/TED.2023.3347209

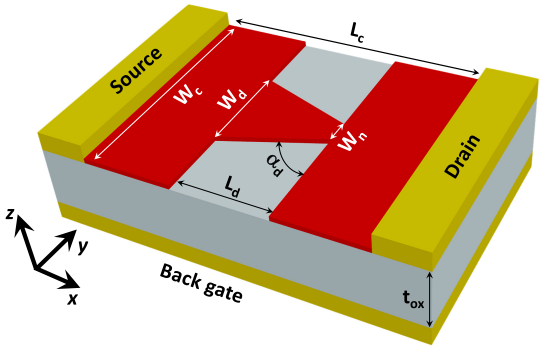

Fig. 1. Sketch of the simulated structure and definition of the geometrical parameters. Shapes in red are graphene. Yellow regions are metallic contacts and back-gate. The gray is the substrate oxide. Above the simulated structure we assume to have air (not shown in the figure).

The ratchet effect in asymmetric electronic structures was proposed over 20 years ago [3], [10] [11], [12]. Recently, interest in these structures has increased due to the importance of the carrier mean free-path (MFP) in these devices. When transport approaches the ballistic regime, geometric effects induce rectifying I–V characteristics [10]. To minimize scattering events that reduce rectification, the MFP should exceed the device length. In this regard, graphene offers unparalleled prospects as an MFP of about 10 μm can be achieved at room temperature [13], [14].

Fig. 1 shows a sketch of the geometric diode that we consider in the present article [2]. It consists of a trapezoidal-shaped graphene structure (red color in the figure) contacted by metals (yellow regions). The graphene layer sits on the dielectric substrate (gray in the figure). Beneath the oxide, a metallic back-gate is used to control the charge density in graphene. Above the structure we assume to have air (not shown in the figure).

The current asymmetry in a device similar to the one shown in Fig. 1 was experimentally reported for the first time in [1] and [2], where authors manufactured a device with a neck aperture $W_n \simeq 75$ nm and a shoulder width $W_c = 400$ nm. The current asymmetry $A \simeq 1.3$ was observed for an applied voltage $V_{DS} = 1.5$ V with exfoliated graphene on SiO_2 substrate with MFP $\simeq 45$ nm. Asymmetry reduced to $A \simeq 1.1$ for CVD graphene with shorter MFP. More recently,

the current asymmetry was experimentally studied as a function of the neck aperture W_n in [15]. With CVD graphene on SiO_2 substrate having MFP $\simeq$ 70 nm, an asymmetry $A \simeq 1.4$ was observed for $W_n = 50$ nm, decreasing to 1.25 for $W_n = 100$ nm. Asymmetry vanished when further increasing W_n. Nguyen et al. [16] could achieve a much larger MFP, thanks to hBN encapsulation. This resulted in an improved asymmetry, up to 1.66 with a neck aperture $W_n = 175$ nm.

In parallel to experimental efforts, several theoretical works have dealt with possible explanations of the current asymmetry. For example, in [17] the asymmetry was explained using the analogy of ballistic transport with classical dilute gas kinetics. Conversely, in [18] the I–V characteristic is calculated treating graphene as 2-D electron gas that satisfies the Dirac equation. The asymmetry mechanism was also investigated through quantum mechanical simulation using a scattering matrix approach [19], hence including coherent transport effects. However, all the aforementioned theoretical contributions assumed a uniform electric field within the device. This neglects more complex field patterns that may arise from the bias at the back-gate terminal. As we will demonstrate below, this assumption is inaccurate, given that electrostatic effects substantially influence the device behavior.

To understand the contributions to rectification and how current asymmetry depends on the geometric parameters and on the bias, we have developed an accurate simulation tool. Carrier transport in single-layer graphene is modeled using a Monte Carlo (MC) approach for the semi-classical electronic transport [20], self-consistently coupled with the solution of the Poisson equation [21]. Carriers respond to the electric field resulting from both the carrier distribution in the graphene layer and the bias on the back-gate contact. We have derived rigorous analytical equations to model carrier motion in graphene. Self-consistency is achieved by alternately simulating charge motion through MC and solving the full 3-D Poisson equation [21]. It is important to note that a similar numerical tool based on the self-consistent Monte Carlo/Poisson simulation was used in [22]. This earlier study used a particle-in-cell algorithm in conjunction with an electron momentum relaxation mechanism. Our approach differs from that of [22] because we add the full 3-D electrostatic. It is worth reiterating that the inclusion of electrostatic effects is crucial for a thorough understanding of the device physics.

The main objective of this article is to provide a clear and comprehensive understanding of the fundamental physics behind the device behavior, rather than the engineering or optimization of its performance. Consequently, we will limit our analysis to ballistic transport and perfectly specular reflections at the graphene edges. Namely, we deliberately neglect the influence of momentum randomizing scattering mechanisms, such as phonon or edge-roughness scattering, which might obscure the basic physics of the device. Moreover, given the symmetric electron and hole transport in graphene, we consider only biases corresponding to a unipolar transport scenario. In particular, we assume a robustly n-type graphene, where hole transport can be safely neglected. In this latter respect, it should be mentioned that a bipolar transport regime occurring at very small carrier densities is in any case detrimental to the current asymmetry. In fact, electrons and holes are driven in opposite directions by a given electric field, so that for both the positive and negative fields we have carriers traveling across the neck region in opposite directions.

As a final remark, we note that while our MC simulator uses a semi-classical transport, one may legitimately wonder whether quantum transport effects (e.g. interference and resonance) can influence the current asymmetry. In this respect, while a quantitative comparison with a quantum transport approach goes beyond the scope of this article, we can share with the readers a few qualitative considerations. Electron interference effects are typically relevant in physical systems or devices that have been conceived and carefully designed to induce such effects. In graphene geometric diodes, however, nothing is designed to induce interference or resonance effects. Instead, the potential energy profile along the transport direction is smooth and does not feature any single or double quantum barrier. In this respect, the *quantum billiard* view of transport in ballistic devices [23] boils down to semi-classical balistic transport (i.e., classical billiard balls). Moreover, even in graphene-based systems where interference effects have been observed [24], [25], [26], this has been reported at deeply cryogenic temperatures, making it unlikely that electron interference effects can have a sizeable influence on the operation of graphene geometric diodes at room temperature, which is the focus of our investigation.

This article is organized as follows. In Section II, we briefly describe the simulation model. In Section III, we show the results of the numerical simulations and the interpretation of the physical phenomena leading to rectification in the device of Fig. 1. Section IV concludes the article.

II. Self-Consistent Monte Carlo 3-D Poisson Simulator

In this section, we briefly describe the numerical code developed for the study of graphene ballistic devices. The motion of carriers is described with the Monte Carlo method, which is self-consistently coupled with the solution of the 3-D Poisson equation.

A. Carrier Transport

Electrons are confined to 2-D trajectories within the graphene plane. By assuming that electrons obey to the semi-classical equation of motion $d\vec{k}/dt = -q\vec{E}/\hbar$ and considering the linear energy dispersion near the K-points $\epsilon = \hbar v_f |\vec{k}|$ [27] with v_f being the graphene Fermi velocity, the equation of motion reads

$$\frac{d\vec{s}}{dt} = \vec{v} = \frac{1}{\hbar}\vec{\nabla}_k \varepsilon\big(\vec{k}(t)\big) = v_f \frac{\vec{k}(t)}{|\vec{k}(t)|} \tag{1}$$

We assume that during the free-flight intervals, the electric field remains constant (i.e., the carrier stays inside a mesh element), so that

$$\vec{k}(t) = \vec{k}_0 + \vec{R}t \tag{2}$$

where $\vec{k}_0$ is the wave vector of the particle at $t = 0$ (beginning of the flight) and, for the sake of a compact notation, we define

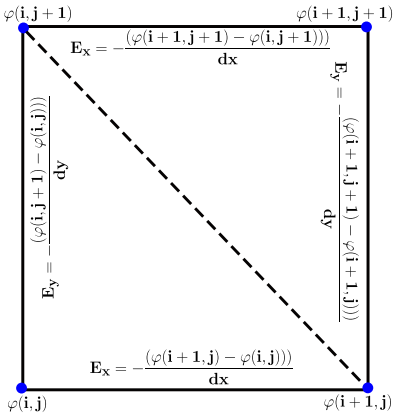

Fig. 2. Sketch of a single pixel of the Poisson mesh. The diagonal divides the rectangular element of a tensor product grid into two triangles. In each triangle, the values of the potential at the vertices uniquely define the electric fields E_x and E_y that are thus constant inside the triangle.

$\vec{R} = -q\vec{E}/\hbar$ where q is the electron charge. Inserting (2) into (1) and integrating over time, the following expression for the trajectory $\vec{s}$ of the particle is found:

$$\vec{s}(t) = \vec{s_0} + v_f\left[\vec{R}\left(\frac{\Psi(t) - A_0}{A_2^2}\right) + - \left(\frac{A_2^2\vec{k_0} - A_1\vec{R}}{A_2^3}\right)\log\left(\frac{u(t)}{u(0)}\right)\right] \tag{3}$$

where $A_0 = |\vec{k_0}|$, $A_1 = \vec{R}\cdot\vec{k_0}$, $A_2 = |\vec{R}|$, $\Psi(t) = (A_0^2 + 2A_1 t + A_2^2 t^2)^{1/2}$, and $u(t) = A_2^2[A_1 + A_2^2 t - A_2\Psi(t)]$. This equation is only valid if the electric field remains constant during the whole flight. The constant field condition is by definition fulfilled in each element of a triangular mesh (see Fig. 2), which we have used for graphene. In particular, the electric field was calculated using the unique plane passing through the vertices of the triangle, according to the expressions also shown in Fig. 2.

The procedure is similar to the simplex Monte Carlo [29]. When a particle begins its free flight within one of these triangles, the duration of the flight is determined by calculating the time of intersection of the particle's trajectory with the edges of the triangular element (by computing the intersection between the trajectory of (3) and the linear equations describing each edge) and selecting the shortest one. At defined time steps, carriers are injected from the device terminals according to the Fermi level of the terminal, following what is done when simulating mesoscopic structures and adapted to MC transport in [31]. The current is

$$\tilde{I}_\alpha = \frac{qW_c}{\pi}\int_0^\infty dE\,\mathrm{Dos}(E)v_f f_\alpha(E) = = \frac{2qW_c}{(\pi\hbar)^2 v_f}\int_0^\infty dE\,\frac{E}{1 + e^{(E - E_{f\alpha})/k_bT}} \tag{4}$$

where k_b is Boltzmann's constant, $\alpha = \{D, S\}$, $\mathrm{Dos}(E) = 2|E|/(\pi v_f^2\hbar^2)$ is the graphene density of states (accounting for spin and valley degeneracy), and $f_\alpha(E)$ the contact Fermi–Dirac distribution where $E_{f\alpha} = q(\varphi_c - V_\alpha)$ is the Fermi level of the contact with φ_c being the average value of the electrostatic potential along the contact line and V_α the bias applied to the contact. In (4), it is assumed that the energy reference is taken at the Dirac point of the contact α, so the injection considers only the conduction band ($E > 0$). When a particle hits a device terminal, it is absorbed. If hitting another boundary, it gets reflected. The net mean current at each contact is calculated as the difference between the injected current and the current associated with the carriers that are absorbed by the contact itself. The potential difference V_{DS} is applied to the contacts as $V_D = V_{DS}/2$ and $V_S = -V_{DS}/2$.

B. Self-Consistency and Evaluation of the Electric Field

To compute the electric field, we solve the Poisson equation. The space charge is determined by the density of electrons. We do not consider graphene chemical doping or charge impurities, either in the graphene or in the back oxide. These factors can induce a fixed charge density. The solution of the Poisson equation is obtained numerically by resorting to a nonuniform-grid finite difference method (FDM). The entire 3-D domain is divided into pixels (the rectangles in Fig. 2) obtained by extruding along the vertical axis the rectangles (elements of a uniform, tensor-product mesh) that we use to discretize the 2-D plane containing the graphene sheet.

We denote as N_x and N_y the number of points used to discretize the graphene plane. Typical dimensions of the devices analyzed are in the order of $W_C \simeq L_C \simeq 100 - 300$ nm. With $N_x \simeq N_y \simeq 100 - 200$, the pixel dimensions are $dx = L_C/N_x \simeq dy = W_C/N_y \simeq 1$ nm. In the vertical dimension, the domain is discretized with N_z points. In our FDM scheme, discretization points along z do not need to be equally spaced. Customarily, we use ten points with $\Delta z = 1$ nm around graphene, and $\Delta z \simeq 10$ nm further away from it. The typical thickness of the oxide substrate in our simulations is $t_{ox} = 100$ nm. We used an air thickness of $t_{air} = 20$ nm in all the simulations presented in this article. We verified that $t_{air} = 20$ nm is sufficiently large to yield results practically independent of this thickness. Therefore, usually $N_z \simeq 20 - 30$ in our simulations. FDM turns the Poisson equation into a sparse linear system with $N_x N_y N_z \simeq 10^6$ unknowns.

Stability issues of the linear formulation of the Poisson equation necessitate an extremely frequent MC-Poisson iteration [21], [28] [30], resulting in a significant increase in computational time. However, for steady-state simulations, stability is guaranteed by using the nonlinear formulation of the Poisson equation that relaxes the time step and spatial mesh limitation of the linear Poisson scheme and avoids unwanted plasma oscillations [21], [28], [30]

$$\nabla\cdot\left(\varepsilon\nabla\varphi^{(k+1)}\right) = \delta(z)qn^{(k)}e^{\frac{q\left(\varphi^{(k+1)} - \varphi^{(k)}\right)}{k_bT}} \tag{5}$$

where the electrostatic potential $\varphi^{(k+1)}$ at the $(k+1)$ iteration is calculated using the electron density $n^{(k)}$ determined by the MC at the kth iteration, with electrons undergoing the kth iteration potential $\varphi^{(k)}$. The $\delta(z)$ function stems from the 2-D nature of graphene, and it can be treated as a field discontinuity along the z dimension in the Poisson equation. In fact, two solutions of Laplace equations are solved below and above graphene. The two solutions are connected by imposing that

at the graphene interface their derivative is discontinuous by an amount equal to the charge density in the graphene. In this approach, there is no need to associate a dielectric constant to the graphene.

We verified that the results do not change if, when solving the Poisson equation, graphene is described as a 3-D volume with a finite thickness of 0.34 nm, and with a constant volumetric charge density along the thickness direction z.

The nonlinear Poisson equation has been discretized obtaining the corresponding FDM matrix equation

$$A\varphi^{(k+1)} = B\left(\varphi^{(k+1)}\right) \tag{6}$$

where A is the discrete Laplacian matrix, and $B(\varphi^{(k+1)})$ is the charge carrier density vector. The potential $\varphi^{(k+1)}$ is computed using a iterative Newton–Rapshon scheme. We used the Neumann boundary conditions for all the borders of the domain, except for the back-gate where a potential of V_{bk} is applied. This assumption implicitly assumes that the work function of metal equals the electron affinity of graphene [31]. The nonlinear Poisson scheme is not affected by self-forces because the field used to move electrons at a given MC iteration is calculated from the potential profile obtained in the previous Poisson step [32]. An electron does not feel the field generated by itself, even if charge and force assignments are not consistent.

III. Results

This section aims to identify the origin of the current asymmetry in the device illustrated in Fig. 1, showing that it arises from a complex interplay between purely electrostatic and geometric effects. To the best of our knowledge, this interplay has not been discussed in the previous literature.

To understand the role of different possible mechanisms inducing a current asymmetry, we analyze the following cases.

1) Uniform electric field regime.
2) Self-consistent simulations with 3-D Poisson.

The first scenario enables us to describe the asymmetry as an effect stemming solely from the device geometry. In the second scenario, the electric field is calculated using the self-consistent MC-Poisson method.

By comparing these two cases, we can highlight the role of electrostatics on the device asymmetry when modifying the device geometry. In all the simulations reported in the following, we consider, as fixed parameters, the following quantities: $\epsilon_{\rm ox} = 3.7\epsilon_0$, $\epsilon_a = \epsilon_0$, $W_c = 100$ nm, $W_d = 40$ nm, and $W_n = 10$ nm.

A. Uniform Electric Field Regime

We examine the case in which the electric field along the y-axis, E_y, is zero, and only the field E_x (assumed to be uniform in the graphene domain) influences carrier transport. The presence of E_x affects the value of the transmission coefficients, T_{ij}, which are defined as the fraction of electrons injected by contact j that are absorbed by contact i.

Three distinct cases, illustrated in Fig. 3, are worth of mentioning.

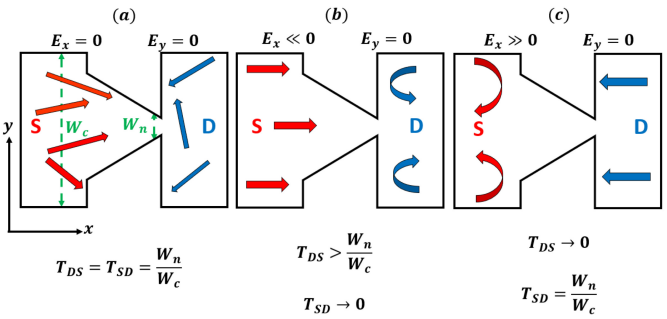

Fig. 3. Schematic representation of the working principle of the geometric diode. Case (a) null electric field E_x. Case (b) negative E_x. Case (c) positive E_x.

Panel a) of Fig. 3 refers to the case of zero applied electric field: $E_x = 0$. In this case, a symmetrical transport condition is expected, resulting in $T_{DS} = T_{SD} = W_n/W_c$.

In contrast, when $E_x \ll 0$ [Fig. 3(b)], strong backscattering occurs for electrons injected from terminal D causing $T_{SD} \to 0$. At the same time, the field guides electrons injected from the S terminal along the x-axis, enhancing the geometric funnel effect. As a result, the transmission T_{DS} reaches values greater than W_n/W_c. In the limit case of $E_x \to -\infty$, the field forces all the electrons entering the funnel region at the aperture W_d to exit the funnel at the aperture W_n (see Fig. 1), resulting in $T_{DS} = W_d/W_c$.

Finally, when $E_x \gg 0$ [Fig. 3(c)], the majority of electrons injected from the S terminal undergo backscattering, leading to $T_{DS} \to 0$. However the asymmetrical shape of the device does not generate an enhancement of the transmission coefficient T_{SD}, which remains equal to W_n/W_c as in $E_x = 0$ case.

To verify the above intuitive trends, MC simulations have been performed by applying a constant electric field $E_x = -V_{DS}/L_C$ throughout the whole graphene shape. In this configuration, the gate-induced electrostatic potential, φ_G, on the graphene plane and the corresponding electron density, n, are given by the solution of the system of two nonlinear equations

$$\varphi_G = \frac{(C_{\rm ox}V_{bk} - qn)}{C_{\rm air} + C_{\rm ox}} \tag{7a}$$

$$n = \int_0^\infty dE\, DoS(E)\, f(E - q\varphi_G) \tag{7b}$$

where $C_{\rm ox}$=($\epsilon_{\rm ox}/t_{\rm ox}$) and $C_{\rm air}$=($\epsilon_{\rm air}/t_{\rm air}$) are the capacitance per unit area of, respectively, the oxide region below and the air region above the graphene layer.

Fig. 4(a) shows the simulated transmission coefficients as a function of the applied voltage V_{DS}, for different values of angle α_d, considering a gate voltage $V_{bk} = 3.38$ V. The angle α_d is varied by changing the length L_d. Using (7), the voltage applied to the back-gate gives rise to the electron density $n = 6.7 \times 10^{11}$ cm^{-2} at $V_{DS} = 0$ V. The corresponding hole density is $p = 1.6 \times 10^{10}$ cm^{-2}, a value small enough to neglect the effect of hole transport.

The results from simulations agree with the intuitive trends discussed above. In particular, for all α_d values, the transmission coefficient T_{SD} tends to $W_n/W_C = 0.1$ for negative values of V_{DS} (i.e., positive E_x), while T_{SD} and T_{DS} tend to zero for

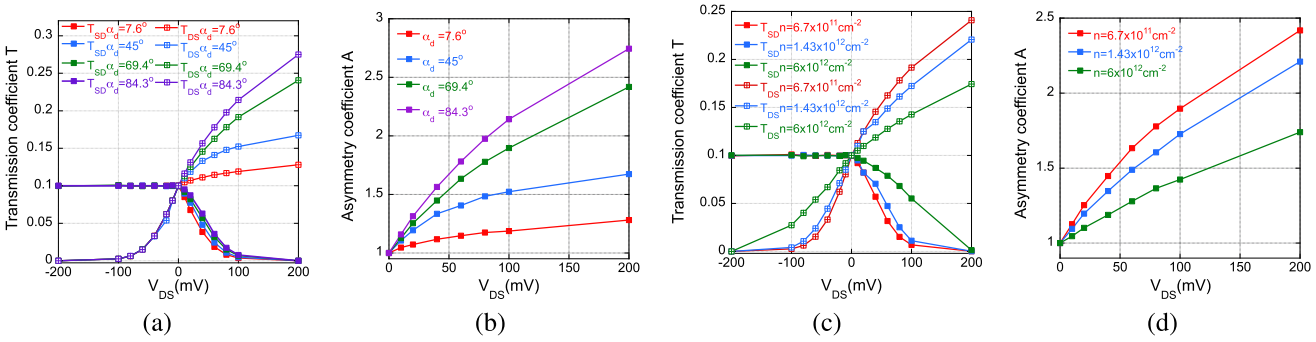

Fig. 4. Uniform electric field regime. (a) Simulated transmission coefficients T_{SD} and T_{DS} as a function of applied voltage V_{DS} for different angles α_d. (b) Asymmetry coefficient as a function of V_{DS} for different angles α_d. (c) Transmission coefficient trend as a function of input voltage V_{DS} for different electron densities. (d) Corresponding asymmetry trend.

negative and positive V_{DS}, respectively. We also note that T_{DS} exceeds W_n/W_C for $V_{DS} > 0$, getting larger and larger as V_{DS} increases, consistently with our previous discussion about the enhancement of the geometric funnel effect that is expected for $E_x \ll 0$.

The net terminal currents I_{DS} can be cast in the form

$$I_{DS}(V_{DS}) = \tilde{I}_S(V_{DS})T_{DS}(V_{DS}) - \tilde{I}_D(V_{DS})T_{SD}(V_{DS}) \quad (8)$$

where $\tilde{I}_{D/S}$ is the current injected through the terminals, as computed through (4). We also define the *current asymmetry coefficient* the quantity

$$A = \frac{I_{DS}(+V_{DS})}{I_{DS}(-V_{DS})} \simeq \frac{T_{DS}(+V_{DS})}{T_{SD}(-V_{DS})} \quad . \quad (9)$$

The above approximation holds as $T_{SD}(V_{DS}) \to 0$ and $T_{DS}(-V_{DS}) \to 0$ for increasing values of $|V_{DS}|$ and $\tilde{I}_S(+V_{DS}) = -\tilde{I}_D(-V_{DS})$ owing to the potential distribution $V_D = V_{DS}/2 = -V_S$.

In the limit of large V_{DS}, the current asymmetry coefficient should tend to W_d/W_n. This result shows that the maximum achievable current asymmetry is simply given by the ratio between the base and the neck of the funnel. In practice, simulations indicate that an unrealistic source–drain voltage $V_{DS} > 10$ V must be applied to have A approach its upper limit. This means that in real devices the geometrical effect is expected to appear modest.

Fig. 4(b) shows the current asymmetry coefficient A [see (9)], as numerically evaluated with MC. It is seen that a rather weak asymmetry ($A \simeq 1.05 - 1.15$) is achieved in the low-voltage regime.

Proper choice of the geometrical parameters allows for optimization. Notably, angle α_d has a particularly relevant impact on the device performance. Fig. 4(a) shows that lower increase in transmission T_{DS} with V_{DS} is observed for $\alpha_d = 7.6°$ than for $\alpha_d = 84.3°$. In the rest of this article, we will denominate *geometrical enhancement* the excess of $T_{DS}(+V_{DS})$ with respect to $T_{SD}(-V_{SD})$ occurring with constant electric field, and solely due to the funnel geometry. When α_d approaches 90°, the shape of the device tends to become symmetric, and the geometrical enhancement drops to 1. The angle $\alpha_d = 84.3°$ considered in the figure is the optimal value that we have identified numerically, namely, the angle resulting in the highest values of the asymmetry coefficient A.

Fig. 4(d) shows that the current asymmetry is also strongly affected by graphene electron density. For this figure, an angle $\alpha_d = 69.4°$ was used. As the electron concentration decreases, the current asymmetry becomes larger. This fact can be explained in a straightforward manner. The Fermi wave vector of electrons in graphene is given by $k_f = (2\pi n)^{1/2}$. Thus, the lower the value of n, the smaller the k_f. To achieve the current asymmetry, externally applied electric field must align the wave vector in the x-direction. The smaller the value of k_f, the more easily this can occur, even with relatively modest electric fields. Note, however, that this simple explanation holds true only until the concentration of electrons is sufficiently larger than the hole concentration. In fact, the effect of the electric field E_x is exactly the opposite for holes and electrons, so that $T_{SD,\text{holes}} = T_{DS,\text{electrons}}$ and $T_{DS,\text{holes}} = T_{SD,\text{electrons}}$. Consequently, when the electrons and holes' concentrations become similar, the current asymmetry disappears.

B. Self-Consistent Simulations

Self-consistent simulations are run by repeatedly alternating 10^5 MC steps with the solution of the nonlinear Poisson equation. The MC time step Δt is chosen so that, on the average, an electron trajectory in one time step is entirely included in a triangular mesh element having a constant electric field, leading to $\Delta t \simeq dx/v_f \simeq dy/v_f \simeq 0.1$ fs. At each MC step, $p_{\text{inj}} = 20$ particles ("virtual electrons") are injected into the simulation domain through each contact (with a statistical weight $w = \tilde{I}_\alpha \Delta t/(q\, p_{\text{inj}})$). The larger the p_{inj}, the more accurate is the solution of the Poisson equation, but the simulation time also becomes longer because the number of particles in the simulation domain increases. In fact, a low number of the particles in Monte Carlo simulations results in possibly large fluctuations of the charge density in the grid elements, because some elements may have very few particles. We found $p_{\text{inj}} = 20$ to be a good tradeoff between accuracy and simulation time.

After having completed a set of 10^5 MC steps, the full 3-D nonlinear Poisson equation [see (5)] is solved. The initial guess for the potential is the solution of (7). As the simulation progresses, the potential is self-updated using the charge distribution provided by the MC solver. The current I_{DS} is calculated after each MC/Poisson iteration and the simulation is stopped when I_{DS} stabilizes.

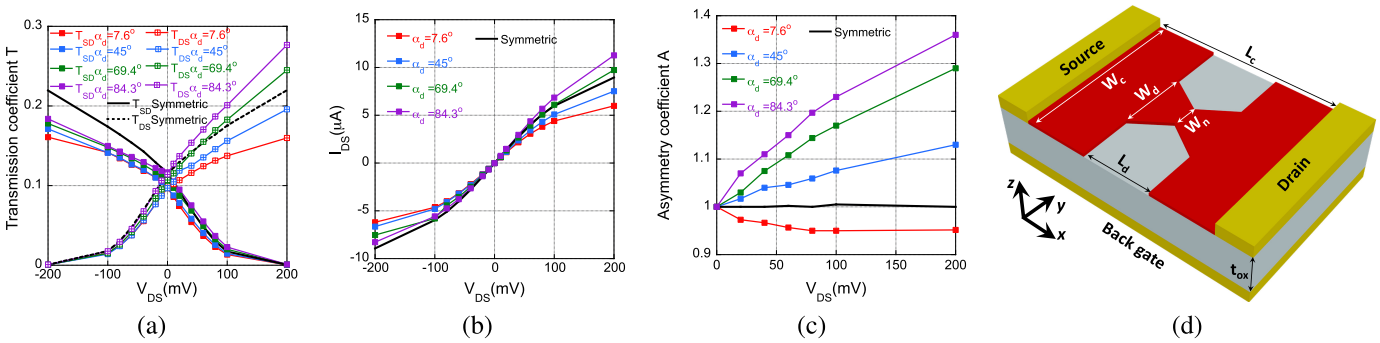

Fig. 5. Self-consistent simulations. (a) Transmission coefficients for various α_d and $V_{bk} = 3.38$ V. (b) Simulated I–V curves for various α_d and $V_{bk} = 3.38$ V. (c) Corresponding current asymmetry trend. (d) Sketch of the symmetric structure indicated with black lines in plots (a)–(c).

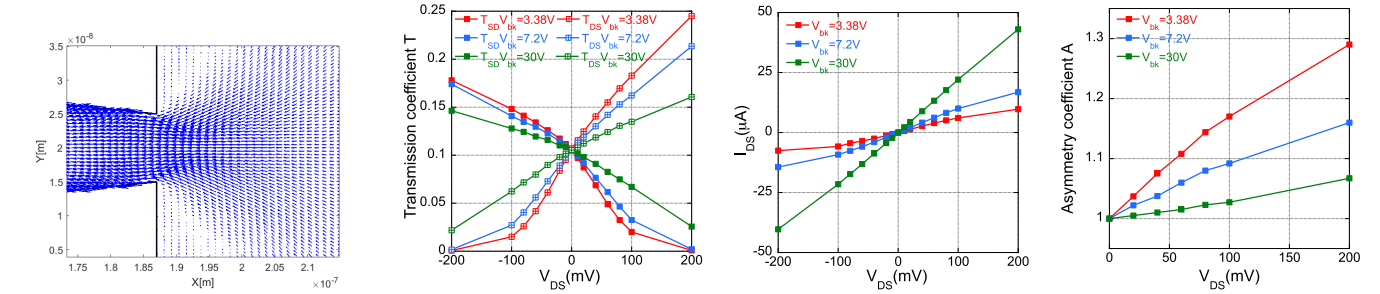

Fig. 6. Self-consistent simulations. (a) Plot of electron flux distribution in proximity of the neck. The plotted configuration considers $V_{DS} = -200$ mV and $\alpha_d = 84.3°$. (b) Transmission coefficients trend considering different V_{bk} and $\alpha_d = 69.4°$. (c) Simulated I–V curves for $\alpha_d = 69.4°$ and different V_{bk}. (d) Corresponding current asymmetry coefficient.

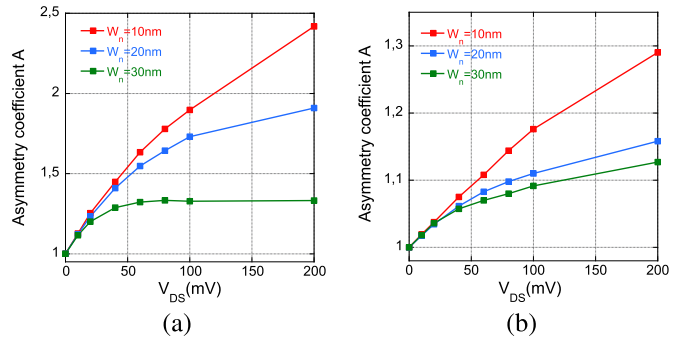

Fig. 7. Trend asymmetry coefficient A for different values of neck W_n considering a gate voltage $V_{bk} = 3.38$ V and $W_d = 40$ nm. (a) Uniform electric field case. (b) Self-consistent case. Note the different scales in the y-axis.

Fig. 5 shows the results of these simulations. Panel d) Fig. 5 shows that a "symmetric" device was also simulated both to check the code and to spot more easily the asymmetry in the I–V curves of the asymmetric devices. Some comments are in order.

As expected, for the symmetric device, the black solid and dashed line are symmetric with respect to V_{DS}. Consistently, the asymmetry coefficient is 1 for all V_{DS}.

A comparison between Figs. 4 and 5 gives the first clear evidence of the role of electrostatic effects. Differently from the case of uniform electric field, in the self-consistent simulations T_{SD} is no longer constant for $V_{DS} < 0$. On the contrary, the more negative the V_{DS}, the larger the T_{SD}. A simple explanation for this fact can be provided. In the vicinity of the neck, the electric field is far from being uniform. Rather, as it is always the case whenever a geometrical spike accumulates charges, near the tips of the neck the electric field becomes concentrated and it is capable of deflecting the trajectory of electrons and channel them into the neck.

This intuitive picture is confirmed by Fig. 6(a) where the electrons flux distribution is plotted in the vicinity of the neck for $V_{DS} = -200$ mV and $\alpha_d = 84.3°$. Electrons are "attracted" toward the neck, and the transmission coefficient T_{SD} can greatly exceed the pure geometrical constraint W_n/W_c (which is equal to 0.1 in these simulations). We will call this effect *electrostatic attraction* in the rest of this article.

A practical consequence of this fact is the severe decrease in the asymmetry coefficient A that may be observed by comparing Figs. 4(b)–5(c): the asymmetry coefficient has almost halved when the full electrostatics is considered.

The electrostatic effects are notably evident when comparing the asymmetry coefficient A versus angle α_d. A distinct difference from the uniform electric field case is observed at $\alpha_d = 7.6°$ [red curves in Figs. 4(b) and 5(c)], where A becomes slightly lower than one. This effect can be understood by looking at the transmission coefficients [red lines in Fig. 5(a)]. T_{SD} (filled squares) at negative V_{DS} is larger than T_{DS} (open squares) at positive V_{DS}, which is opposite to the behavior observed for a uniform electric field [red curves in Fig. 4(a)]. The difference is entirely due to the electric field, which is no longer uniform, in particular at the neck. The *electrostatic attraction* has now come into play, and it is larger than the *geometrical enhancement*, causing a net asymmetry coefficient $A < 1$. Electrostatic effects influence T_{SD} and T_{DS}

even at $V_{DS} = 0$, causing a slight deviation from W_n/W_c for all angles α_d considered.

Fig. 6 completes the analysis for the full self-consistent case. These figures report the transmission coefficient, the I–V curves, and the asymmetry coefficient A for $\alpha_d = 69.4°$ at varying V_{bk}. As V_{bk} increases, a greater number of carriers become available for transport (resulting in a higher electron density). Consequently, the transmission coefficient decreases in accordance with the earlier discussion regarding the Fermi wave vector of electrons in graphene and the strength of the electric field required to align particle trajectories parallel to the x-axis. Curves tend to become more and more linear, with higher slope due to the increased number of carriers being available for the transport. This increased linearity implies a lower asymmetry coefficient as it can be seen in Fig. 6(d).

An analysis of the asymmetry coefficient A for various neck widths, W_n, has also been conducted. The same back-gate voltage ($V_{bk} = 3.38$ V) and shoulder width ($W_d = 40$ nm) used in the previous analysis were considered. The results are presented in Fig. 7, where the left and right panels correspond, respectively, to a uniform field and a self-consistent simulation.

Although a direct comparison with the experimental results in [15] is not possible because ballistic transport conditions are assumed in this article, our numerical results are qualitatively consistent with the experiments. Indeed, a reduction in the asymmetry coefficient for increasing values of the neck aperture, W_n, was reported in [15]. Moreover, asymmetry values around 1.25–1.40 were reported for an applied voltage of 2 V in devices with a length in the micrometer range [15]. Our simulations show comparable asymmetry values for an applied voltage of 200 mV and a device length in the range of hundreds of nanometers, namely, for electric fields comparable to those in [15].

Another comparison can be made with the experimental results in [16], where asymmetry was shown to reduce when increasing the gate voltage, which is also predicted by our simulations [see Fig. 6(d)].

Finally, we have analyzed the behavior of current asymmetry A versus. the value ϵ_r of the substrate dielectric constant (not shown). In these simulations, we set $V_{bk} = 3.38$ V and adjusted the substrate thickness so as to maintain the same induced charge density on graphene. We observed that A decreases for increasing ϵ_r. One should further consider that depositing the graphene sheet on top of high-k dielectrics results in a significant mobility degradation [33], [34] [35], [36], i.e., shorten mean-free path. Addressing this point in detail requires the inclusion of remote polar phonons in simulation future work.

IV. Conclusion

In this article, the interpretation of asymmetric current–voltage characteristics in geometric diodes has been revisited by exploiting a sophisticated self-consistent Monte Carlo/3-D Poisson simulation tool, which has been developed *ad hoc*. The behavior of the device in terms of transmission coefficients from drain to source (and vice versa) and current in the two terminals has been analyzed in two different scenarios. First, the case of a constant electric field across the device has been considered. Then, the self-consistent case has been addressed, where the electric field is determined by the charge distribution in graphene and the voltage applied to the back-gate contact.

By comparing the two scenarios, we could demonstrate that the evaluation of the device rectification based only on geometry asymmetry is incomplete. In fact, electrostatic effects, in particular the charge-induced electric field near the diode's neck, influence significantly the device operation and can cancel or even reverse the rectification due to the geometric asymmetry.

Our interest in this article was to describe the physical phenomena taking place in the geometric diode, rather than engineering its performance, and hence, our analysis is not exhaustive in determining the actual potential of the device in terms of rectification. Nevertheless, our simulations could identify important information for the device design: 1) the analysis of the device under a uniform field condition tends to overestimate the rectifying capabilities of the geometric diode and 2) the asymmetry coefficient tends to improve as the funnel angle α_d increases, with a maximum asymmetry occurring for $\alpha_d \simeq 85°$. A more comprehensive analysis of the device performance is left for a future work, where we would like to include the effect of scattering due to local and remote phonons (the latter significantly reducing the mobility in graphene deposited on polar dielectrics with respect to freestanding graphene) and graphene edge roughness, as well as address the high-frequency behavior, which is of paramount importance for many perspective applications.

References

[1] G. Moddel, Z. Zhu, S. Grover, and S. Joshi, "Ultrahigh speed graphene diode with reversible polarity," *Solid State Commun.*, vol. 152, no. 19, pp. 1842–1845, Oct. 2012.

[2] Z. Zhu, S. Joshi, S. Grover, and G. Moddel, "Graphene geometric diodes for terahertz rectennas," *J. Phys. D, Appl. Phys.*, vol. 46, no. 18, May 2013, Art. no. 185101.

[3] A. M. Song, "Electron ratchet effect in semiconductor devices and artificial materials with broken centrosymmetry," *Appl. Phys. A, Solids Surf.*, vol. 75, no. 2, pp. 229–235, Aug. 2002.

[4] G. Auton et al., "THz detection and imaging using graphene ballistic rectifiers," *Nano Lett.*, vol. 17, pp. 7015–7020, Jan. 2017.

[5] R. A. Lewis, "A review of terahertz detectors," *J. Phys. D, Appl. Phys.*, vol. 52, Mar. 2019, Art. no. 433001.

[6] A. Luukanen, R. Appleby, M. Kemp, and N. Salmon, "Millimeter-wave and terahertz imaging in security applications," *THz Spectrosc. Imag.*, vol. 171, pp. 491–520, Oct. 2012.

[7] X. Yin, B. W.-H. Ng, and D. Abbott, *Terahertz Imaging for Biomedical Applications*. Cham, Switzerland: Springer-Verlag, 2012.

[8] A. I. McIntosh, B. Yang, S. M. Goldup, M. Watkinson, and R. S. Donnan, "Terahertz spectroscopy: A powerful new tool for the chemical sciences?" *Chem. Soc. Rev.*, vol. 41, no. 6, pp. 2072–2082, 2012.

[9] Y. Huang, Y. Shen, and J. Wang, "From terahertz imaging to terahertz wireless communications," *Engineering*, vol. 22, pp. 106–124, Mar. 2023.

[10] A. M. Song, A. Lorke, A. Kriele, J. P. Kotthaus, W. Wegscheider, and M. Bichler, "Nonlinear electron transport in an asymmetric microjunction: A ballistic rectifier," *Phys. Rev. Lett.*, vol. 80, no. 17, pp. 3831–3834, Apr. 1998.

[11] H. Linke, W. Löfgren, H. Xu, P. Omling, and P. E. Lindelof, "A quantum dot ratchet: Experiment and theory," *Europhys. Lett.*, vol. 45, no. 3, p. 406, Feb. 1999.

[12] A. M. Song et al., "A nonlinear transport device with no intrinsic threshold," *Superlattices Microstruct.*, vol. 25, nos. 1–2, pp. 269–272, Jan. 1999.

[13] K. I. Bolotin et al., "Ultrahigh electron mobility in suspended graphene," *Solid State Commun.*, vol. 146, nos. 9–10, pp. 351–355, Jun. 2008.

[14] L. Banszerus et al., "Ballistic transport exceeding 28 μm in CVD grown graphene," *Nano Lett.*, vol. 16, no. 2, pp. 1387–1391, Feb. 2016.

[15] H. Wang et al., "CVD-grown monolayer graphene-based geometric diode for THz rectennas," *Nanomaterials*, vol. 11, no. 8, p. 1986, Aug. 2021.

[16] V. H. Nguyen et al., "Optimum design for the ballistic diode based on graphene field-effect transistors," *NPJ 2D Mater. Appl.*, vol. 5, no. 1, p. 89, Dec. 2021.

[17] P. Zhang and D. M. H. Hung, "An analytical model for ballistic diode based on asymmetric geometry," *J. Appl. Phys.*, vol. 115, no. 20, pp. 204908-1–204908-5, May 2014.

[18] D. Dragoman and M. Dragoman, "Geometrically induced rectification in two-dimensional ballistic nanodevices," *J. Phys. D, Appl. Phys.*, vol. 46, no. 5, Feb. 2013, Art. no. 055306.

[19] D. Mencarelli, G. M. Zampa, and L. Pierantoni, "Current-voltage characterization of multi-port graphene based geometric diodes for high-frequency electromagnetic harvesting," *IEEE Access*, vol. 10, pp. 123251–123258, 2022.

[20] C. Jacoboni and L. Reggiani, "The Monte Carlo method for the solution of charge transport in semiconductors with applications to covalent materials," *Rev. Mod. Phys.*, vol. 55, no. 3, pp. 645–705, Jul. 1983.

[21] P. Palestri, N. Barin, D. Esseni, and C. Fiegna, "Stability of self-consistent Monte Carlo simulations: Effects of the grid size and of the coupling scheme," *IEEE Trans. Electron Devices*, vol. 53, no. 6, pp. 1433–1442, Jun. 2006.

[22] J. Stearns and G. Moddel, "Simulation of Z-shaped graphene geometric diodes using Particle-in-Cell Monte Carlo method in the quasi-ballistic regime," *Nanomaterials*, vol. 11, no. 9, p. 2361, Sep. 2021.

[23] C. W. J. Beenakker and H. van Houten, "Billiard model of a ballistic multiprobe conductor," *Phys. Rev. Lett.*, vol. 63, no. 17, pp. 1857–1860, Oct. 1989.

[24] P. Gehring et al., "Quantum interference in graphene nanoconstrictions," *Nano Lett.*, vol. 16, no. 7, pp. 4210–4216, Jul. 2016.

[25] F. Miao, S. Wijeratne, Y. Zhang, U. C. Coskun, W. Bao, and C. N. Lau, "Phase-coherent transport in graphene quantum billiards," *Science*, vol. 317, no. 5844, pp. 1530–1533, Sep. 2007.

[26] S. Russo et al., "Observation of aharonov-bohm conductance oscillations in a graphene ring," *Phys. Rev. B, Condens. Matter*, vol. 77, no. 8, Feb. 2008, Art. no. 085413.

[27] A. H. C. Neto, F. Guinea, N. M. R. Peres, K. S. Novoselov, and A. K. Geim, "The electronic properties of graphene," *Rev. Mod. Phys.*, vol. 81, no. 1, pp. 109–162, 2009.

[28] D. Esseni, P. Palestri, and L. Selmi, *Nanoscale MOS Transistors: Semi-Classical Transport and Applications*. Cambridge, U.K.: Cambridge Univ. Press,2011.

[29] J. Bude and R. K. Smith, "Phase-space simplex Monte Carlo for semiconductor transport," *Semicond. Sci. Technol.*, vol. 9, no. 5S, pp. 840–843, May 1994.

[30] P. Palestri, N. Barin, D. Esseni, and C. Fiegna, "Revised stability analysis of the nonlinear Poisson scheme in self-consistent Monte Carlo device simulations," *IEEE Trans. Electron Devices*, vol. 53, no. 6, pp. 1443–1451, Jun. 2006.

[31] P. Palestri, L. Lucci, S. D. Tos, D. Esseni, and L. Selmi, "An improved empirical approach to introduce quantization effects in the transport direction in multi-subband Monte Carlo simulations," *Semicond. Sci. Technol.*, vol. 25, no. 5, May 2010, Art. no. 055011.

[32] S. E. Laux, "On particle-mesh coupling in Monte Carlo semiconductor device simulation," *IEEE Trans. Comput.-Aided Design Integr. Circuits Syst.*, vol. 15, no. 10, pp. 1266–1277, Feb. 1996.

[33] S. Fratini and F. Guinea, "Substrate-limited electron dynamics in graphene," *Phys. Rev. B, Condens. Matter*, vol. 77, no. 19, May 2008, Art. no. 195415.

[34] V. Perebeinos, S. V. Rotkin, A. G. Petrov, and P. Avouris, "The effects of substrate phonon mode scattering on transport in carbon nanotubes," *Nano Lett.*, vol. 9, no. 1, pp. 312–316, Jan. 2009.

[35] A. Konar, T. Fang, and D. Jena, "Effect of high-κ gate dielectrics on charge transport in graphene-based field effect transistors," *Phys. Rev. B, Condens. Matter*, vol. 82, no. 11, Sep. 2010, Art. no. 115452.

[36] Z.-Y. Ong and M. V. Fischetti, "Theory of interfacial plasmon-phonon scattering in supported graphene," *Phys. Rev. B, Condens. Matter*, vol. 86, no. 16, Oct. 2012, Art. no. 165422.